Comparative Study of Oxide Speciation in Steel by Inert Gas Fusion Technique

Pavel V. Krasovskii* , Wolfgang Gruner, Konstantin V. Grigorovitch***

* Baikov Institute of Metallurgy and Materials Science, Russian Academy of Sciences; Moscow, Russia;
** Leibniz-Institute for Solid State and Materials Research, Dresden, Germany

The paper presents the application of an improved procedure for oxide speciation in steels by temperature ramped inert gas fusion technique on commercially available instruments. Main steps of analysis, data processing and interpretation of the results are described. The effects of instrumentation and auxiliary materials on the evolution kinetics of oxygen during an analysis are emphasised. The procedure is applied to determine the content of alumina and spinel species in high-carbon steels, attested as reference materials. The results of the gas fusion technique are correlated to those of the chemical analysis and scanning electron microscopy equipped with energy dispersive X-ray detector.

Keywords: gas fusion analysis, oxygen determination, species analysis, oxide inclusions, steel cleanliness.

Introduction

Inert gas fusion analysis (GFA) or carrier gas hot extraction is one of the thermal evolution methods, routinely used in industry to determine the oxygen content of steel products. This technique involves sample fusion in a graphite crucible under flowing helium, oxygen extraction from a melt as CO, catalytic oxidation of CO to CO_2 over heated rare earth copper(II) oxide and detection of CO_2 by the infrared (IR) absorption. Total oxygen content is determined in the isothermal mode at temperatures above 2500 K. The complete simultaneous extraction of all oxygen species from a sample usually proceeds in 30-40 seconds. The procedure is developed in details and a large number of reference materials is available.

The working characteristics of steel products are, however, determined not only by the total concentration of oxygen but also by its chemical state within steel matrix, namely by its distribution between different oxide species, such as chromite, silicates, alumina etc. Therefore, since the 1980s attempts have been made to elaborate the gas fusion technique for separation of different oxide species by applying monotonous or step-wise heating. R. Prumbaum et al. [1] were the first who considered the temperature ramped inert gas fusion technique with IR detector. The authors proposed the physico-chemical model of oxides reduction and the approach to the interpretation of the evolution curves. The reduction sequence of oxides was derived from their values of the standard Gibbs energy of formation. Using the custom-built apparatus, the rate and temperatures of the silica reduction were studied as a function of pressure in a gas phase of analyser, silicon content and heating rate. Later, the successful employment of the commercial LECO RO-316 analyser was reported for oxide separation in steels and slags [2,3]. Instead of the temperature ramping, which did not provide complete separation of peaks of steel samples, H. Hocquaux et al. [4] proposed a step-wise heating. They also discussed instrumental improvements such as temperature control, design of extraction furnace, sensitivity of IR detectors. The proper sampling technique for the purpose of gas analysis was emphasised in [5]. In this work the temperature ramping was applied to determine the content of oxidic oxygen of several steel grades. This was closely correlated to the micro-cleanliness of steel, expressed in terms of the frequency of oxides inclusions on cross-sections. The separation of the bulk oxygen and surface oxide film in ultra-clean steels by stepwise heating was reported in [6]. A similar procedure was earlier applied for silicon [7].

The progress of earlier works has not, however, succeeded in an extensive practical use of the temperature ramping technique, available in modern analysers. This fact was mainly attributed to two problems. The first one was the absence of numerical algorithm and software for processing of raw kinetic data. As the evolution curves of real steels represented the superposition of overlapped peaks, a proper deconvolution procedure was necessary to quantify the amount of oxide species. The second problem concerned the start temperatures of carbothermal reduction of oxide species T_s. Considerable discrepancy existed regarding the equilibrium and real values of T_s. This was explained by non-equilibrium conditions of gas fusion reactions and the use of thermodynamic prediction was open to question [4].

The above problems have been worked on in the last years. At first, K. V. Grigorovitch et al. [8,9] have developed an OxSep original software to process the results of temperature ramped analysis. The numerical procedure involved consecutive separation and subtraction of individual peaks from a total evolution curve. The temperature-dependent background evolution as well as mixing effects in a gas system of analyser were also treated by this model. Then, P.V. Krasovskii et al. [10] have improved the thermodynamic model of carbothermal reduction of oxide inclusions within a molten sample, saturated with graphite. The equilibrium values of T_s were recalculated for silica and alumina in iron matrix. The model prediction was found to be in reasonable agreement with experimental data for chemically pure oxide species. The aim of this work was to apply the improved procedure for oxide speciation in high-carbon steels, to study the effects of instrumentation and crucibles on the evolution kinetics, to correlate the analysis results with those, obtained by other methods. High-carbon steels were chosen as object of analysis, because their cleanliness is greatly reduced by rigid high-alumina inclusions [11].

Experimental

Samples. Two samples of high-carbon steels in the form of rods (d=10 mm), referred as SG1 and SG4, and another sample of rimmed steel with protective nickel coating, referred as SG15, were used in this study. The above samples were supplied as reference materials for gas fusion analysis (Ural Institute of Metals, Russia). The chemical composition of the materials is given in **table 1**. The oxide inclusions in SG1 and SG4 samples were determined in a preliminary investigation using chemical analysis and scanning electron microscopy equipped with energy dispersive X-Ray detector (SEM/EDX). The materials were, firstly, dissolved anodically to collect and determine the amount of oxide precipitates of different types using the classical procedures of "wet" chemistry. The results, summarised in **table 2**, show that the deoxidation products consist mainly of alumina and silicates. In SG4 material a noticeable amount of Mg- or Ca-containing oxides was found. The presence of iron oxides in SG1 material, which is deoxidized with aluminium, is open to question. The oxide inclusions were also observed under optical microscope on polished longitudinal sections. The particles found in both samples were divided into two groups: small glassy globules and large taupe acute-angled grains. Some large clusters were broken during rolling and appeared as aligned blocky fragments. The typical oxide species were identified using Leo 430 microscope with an Oxford ISIS EDX analysis system. The SEM photographs of the alumina and spinel precipitates along with EDX spectra are shown in **figures 1 and 2**. In SG1 material the taupe acute-angled particles were found to be alumina while in SG4 material two types of high-alumina inclusions could be distinguished. As can be seen from **table 3** the first one was composed of alumina containing Mg as impurity while the second one corresponded rather to spinel $MgO{\cdot}Al_2O_3$. These two groups also differed in particle size, which was noticeably larger for spinel inclusions. Most of oxide inclusions were covered by a shell of sulphides. These were MnS in SG1 material while in SG4 material both CaS and MnS could be detected. The presence of Mg-containing inclusions in SG4 material is in agreement with the results of chemical analysis. However, Mg does not form an individual MgO phase, but enters spinel. In general, the oxide inclusions in SG1 and SG4 materials are very similar to those which have often been found in high-carbon steels and repeatedly described in literature.

Instruments. Measurements were made simultaneously on TC-436DR and TC-436 (LECO, USA) commercial analysers in different laboratories. The design of the extraction furnaces, oxidizing heaters and sensitivity of IR detectors of these instruments were the same. The main difference concerned the flow diagrams, which are shown in **figure 3**. In TC-436 system purified carrier gas (helium) flowed consecutively through the extraction furnace (3), oxidizing heater (4) and, then, into IR (6) and TC (9) cells, which were arranged in a row. In TC-436DR system helium stream after passing through the extraction furnace split into

Table 1. Chemical composition (in wt%) of steel reference materials.

	O total	C	Mn	Si	Al	Cr
SG1	0.003 ± 3	0.47	0.59	0.20	0.027	0.20
SG4	0.0033 ± 2	0.98	0.24	0.38	0.029	1.18
SG15	0.024 ± 13	0.14	0.50	0.07	-	0.15

Table 2. The amount (in μg/g) of oxide precipitates in SG1 and SG4 materials after electrochemical isolation.

Sample	Total	SiO_2	Al_2O_3	FeO	MgO+CaO	MnO	Others
SG1	130	12	88	26	<1	1	-
SG4	103	8	68	3	15	-	9

Table 3. Chemical composition of high-alumina particles in SG4 reference material with SEM/EDX analysis (oxygen and iron were excluded before normalisation; 17 particles in total).

	Size	Composition [at.%]					
	[μm]	Mg	Al	Si	S	Ca	Mn
min-max	1-4	1-9	62-82	0-3	6-14	1-12	3-9
min-max	7-30	18-21	61-81	0-1	0-10	0-7	0-3

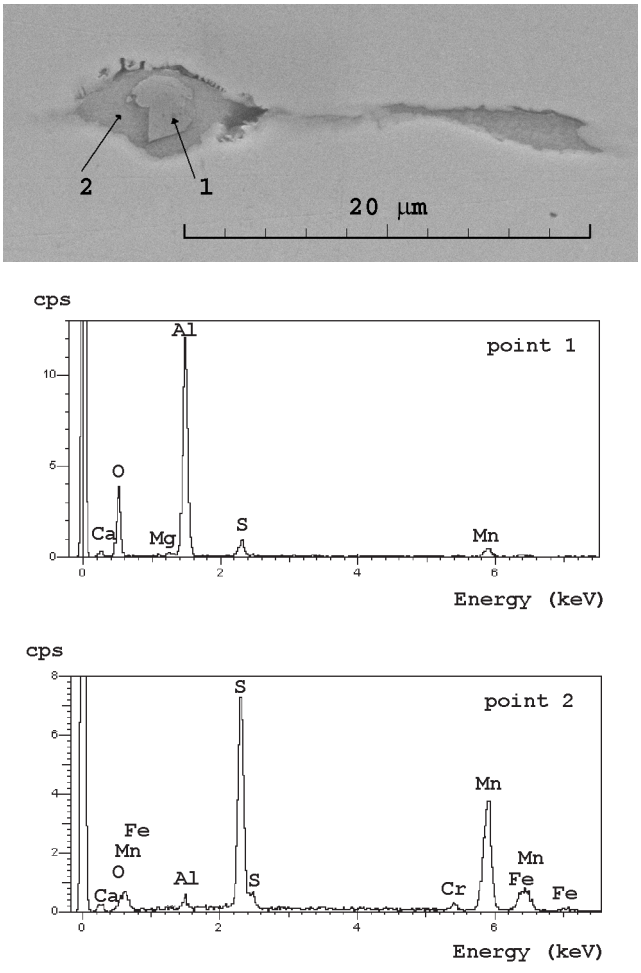

Figure 1. Al_2O_3 particle inside an MnS shell; SG4 material; (a) view from scattered electrons, (b,c) EDX spectra of points 1 and 2, respectively.

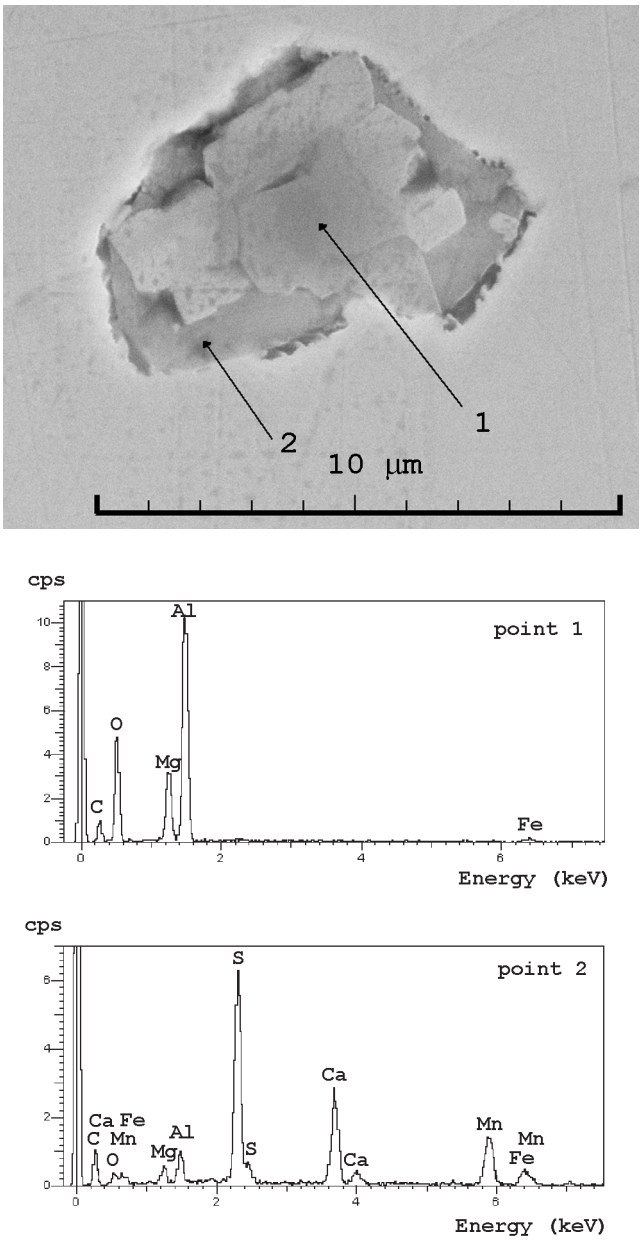

Figure 2. Spinel particle inside a CaS-MnS shell; SG4 material; (a) view from scattered electrons, (b,c) EDX spectra of points 1 and 2, respectively.

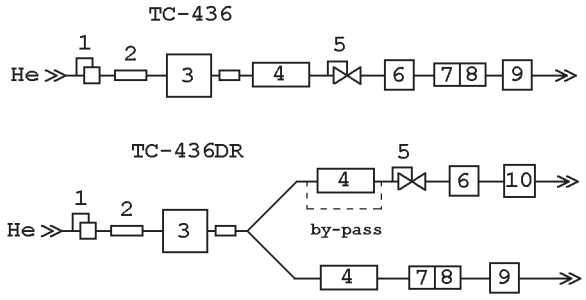

Figure 3. Flow diagrams of TC-436 and TC-436DR analysers (LECO); 1 – pressure regulator, 2 – flow meter, 3 – extraction furnace, 4 – oxidising heater, 5 – flow regulator, 6 – CO_2 IR-detector, 7 – lecosorb, 8 – anhydrone, 9 – N_2 TC cell, 10 – CO IR-detector.

two paths so that oxygen and nitrogen were measured in parallel lines. In both cases the helium flow rate, entering the extraction furnace, was regulated to about 300 ml/min. However, due to parallel flow diagram the analytical flow rate in each analytical line of TC-436DR system was about halved.

Crucibles. A double crucible technique was applied. The outer crucible played a role of a heater providing a uniform temperature field. The inner crucible served as a reactor for sample fusion. Two batches of crucibles of the same type (Part No. 775-433/775-431) were obtained from LECO. One of the batches was produced in the USA, the other one in England. Due to differences in manufacturing technology, they had different properties. Namely, the crucibles from the USA had a lighter weight, thinner walls and higher heating ability. But the most important characteristic was found to be the crucible porosity, which had a strong impact on the oxygen evolution kinetics during an analysis. The crucibles produced in the USA had a higher porosity as well as a larger size of pores. Using image analysis program the porosity values were calculated to be 18 and 6 % for crucibles from the USA and the UK, respectively.

Temperature calibration. In most commercial Oxygen/Nitrogen analysers the furnace temperature is controlled via power consumption rather than directly monitored with pyrometer. The real temperature is recalculated with power-temperature calibration curves. In the present work the temperature calibration was performed as follows. After two outgas cycles (2500 K; 10s) pieces of copper (≈ 0.2 g), silicon (≈ 0.05 g) or platinum (≈ 0.05 g) were dropped into a crucible and heated at the rate about 1 K/s. By observing samples through the window above the crucibles, the melting points were fixed. These corresponded to eutectic points of Cu-C (1358 K) [12], Si-C (1677 K) [12] and Pt-C (1978 K) [13] phase diagrams. Three outer crucibles of each type from the same batch were tested. The data obtained were used to refine the *factor* and *offset* coefficients in the calibration equation, cited in LECO documentation for EF-400 furnace:

$$T = factor \cdot \{offset + f(p)\}, \quad (1)$$

where $f(p) = 613 \cdot p - 0.0427 \cdot p^2$ (p in kW). The calibration curves are shown in **figure 4**, where it can be seen that the thin-walled porous crucibles from the USA have a higher heating power. The uncertainty of temperature control is estimated to be within ± 30 K. This is quite acceptable for current analytical purposes.

Measuring procedure. The rods of SG1 and SG4 materials were cut into pieces of one gram. SG15 samples were supplied as nickel-plated cylinders of 0.4 g. Just before analysis SG1 and SG4 samples were abraded by a file and annealed in the extraction furnace under helium stream (1300 K; 60 s). SG15 samples were analyzed immediately after cleaning in ethanol. After sample loading into jaw arrangement and crucible replacement the system was purged by helium (298 K; 20 s) followed by double outgas

cycles (2700 K; 10 s) and analysis delay for base line stabilization (60 s; analysis delay comparator = 0.05). The furnace power was ramped at a rate 6 Watt/s, producing a heating rate about 2 K/s. Analysis start temperature was 1350-1390 K, the analysis time was up to 400 s (maximum allowed).

Data processing. The intensity values of IR-detector I [a.u.] were averaged by 10 points and smoothed by iterative moving average filter (3 adjacent points; 50-100 iterations). When smoothing, the absolute deviation between smoothed and initial values was controlled to be within ± 1 a.u. (twice as high as AD step). The power values were fitted by a straight line and recalculated to the temperature values with Eq.(1). Then, the IR intensities were shifted relative to the temperature values on the delay time (7-10 s), viz. the time for the gaseous sample to reach the IR detector. The temperature-dependent background gas release is caused by contaminants in both carrier gas and graphite crucibles as well as water vapours adsorbed on the walls of tubing and furnace. The system background is usually not exactly known as it can be only observed when analysing the oxygen-free sample of the same matrix. In general, the background must be lower than the blank, which is measured with empty crucibles. Based on many experiments the following empirical function was found to give a fair representation of the background evolution under heating at constant rate [9]:

$$I_b(T) = \frac{h}{1 + e^{-\frac{4[T-0.5(T_o+T_1)]}{T_1-T_o}}}, \qquad (2)$$

where T – current temperature, T_o and T_1 – characteristic temperatures. **Figure 5** illustrates the evolution kinetics of oxygen from a synthetic sample of iron, containing 0.5 wt.% C and 0.7 wt.% Si. Here, about 40 μg/g of oxygen is bound to silica inclusions, which produce a single peak on the evolution curve. "T_{start} of silica" refers to the equilibrium temperature of silica reduction, which was calculated with a thermodynamic model (vide infra). This value corresponds well to the position of the silica peak. It is clearly seen that at the end of the analysis the evolution rate does not diminish to zero, but remains at some steady level h. According to Eq. (2) the background rate increases most intensively at $T = (T_o + T_1)/2$, while above T_1 it becomes relatively stable, approaching h. Depending on the heating rate, sample chemistry and other factors, the values of the characteristic temperatures T_o and T_1 are usually selected within the range 1400-1800 and 1800-2200 K, respectively. The tentative values T_o and T_1 must be found in a series of blank runs prior to measurements. Then, they can be corrected to ensure the consistency between the values of the total oxygen content, obtained in both isothermal and ramping modes. In the present work the background evolution contributed about 10-30 % to the total amount of oxygen detected. When analysing steel samples with lower oxygen content, the use of an external gas refining system might be essential to reduce the background and to increase the signal-to-noise ratio [14].

The background-corrected curves were plotted on the temperature mesh with the step of 5 K and scaled as follows:

$$y(T), \mathrm{K}^{-1} = \frac{cal}{F \cdot W} \frac{I(T)}{r(T)}, r > 0, \qquad (3)$$

where cal is calibration factor, W [g] sample weight, r [K/s] local heating rate, F [a.u.·s/g] – sensitivity coefficient of IR-detector ($F = 1.13 \cdot 10^8$ for CO_2 cell). Then, the oxygen content released in the range from T_o up to T_1 can be calculated as follows:

$$c_O^{T_o-T_1}, \% = 100 \cdot \int_{T_o}^{T_1} y(T)dT\,. \qquad (4)$$

he bulk content of oxygen was calculated by integrating $y(T)$ from the start temperature of the sample melting. The

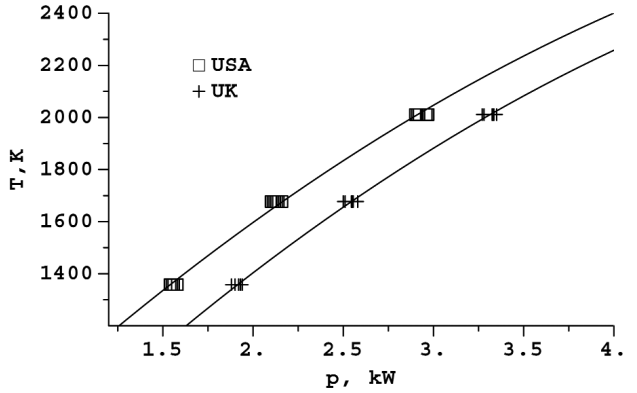

Figure 4. Temperature calibration curves, obtained from TC-436DR system using crucibles Part No. 775-433/775-431 of different producers.

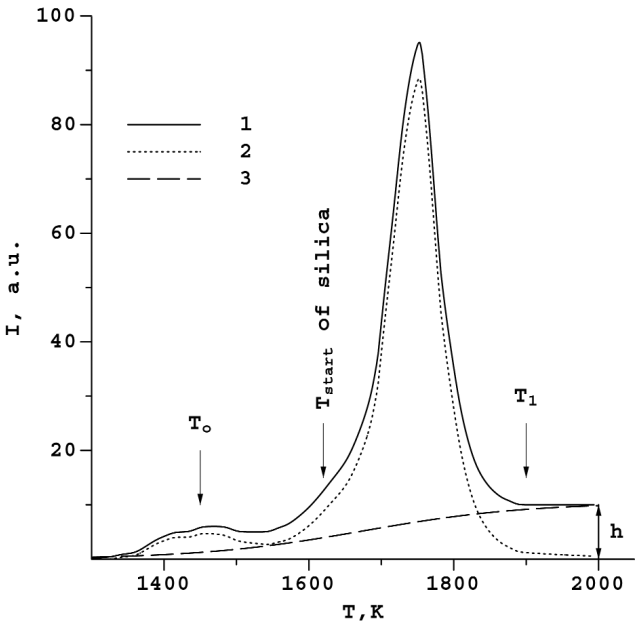

Figure 5. Background correction: 1 – raw curve, 2 – corrected curve, 3 – background function (Eq.2); the sample of iron containing 0.5 wt.% C, 0.7 wt.% Si and 40 μg/g O.

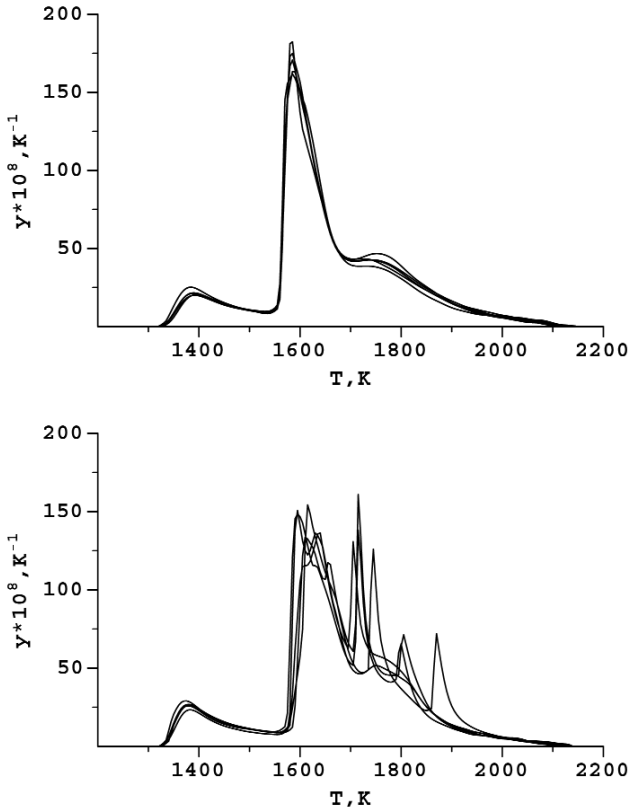

Figure 6. Evolution kinetics of oxygen from SG15 material in (a) porous and (b) dense crucibles, recorded with TC-436DR analyser.

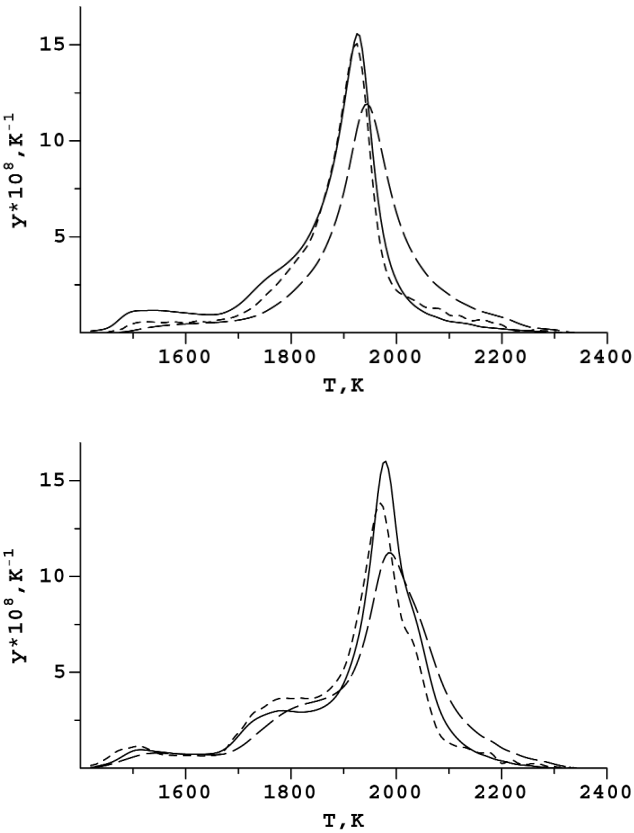

Figure 7. Apparatus effect on the evolution kinetics of oxygen from (a) SG1 and (b) SG4 samples in porous crucibles; *solid line* - TC436 raw data, *dash line* - TC436DR raw data, *dot line* - TC436DR curves after correction by Eq.5.

surface oxygen was assumed to be released by a solid sample.

Results and discussion

Effects of crucible and apparatus on the evolution kinetics. The application of GFA for oxygen speciation in steels shows that both apparatus and graphite crucibles may have an impact on the observed evolution kinetics. The effect of inner crucibles is caused by the difference in their porosity. This can be clearly seen from **figure 6**, which illustrates the evolution curves of oxygen from SG15 material in porous (USA) or dense (UK) inner crucibles. Oxygen evolution in porous crucibles proceeds smoothly with excellent repeatability, while in dense crucibles the reaction kinetics becomes erratic, deteriorated with sharp random peaks. The observed phenomenon involves the mechanism of CO bubbles removal from the molten sample. Bubbles are initially nucleated on the surface of oxide particles in the bulk of the melt. Some of the bubbles float immediately to the melt surface but some of them adhere to the crucible walls. If the crucible porosity is high, the gas from attached bubbles can easily leave the melt/graphite interface by infiltrating through pores and cracks in the walls. However, on the walls of dense crucibles bubbles grow until the buoyancy exceeds the attachment force (surface tension of the melt). To confirm this mechanism the analysis runs were aborted and the bottom surface of the samples was inspected under a stereo-microscope. In the case of dense crucibles the traces of attached bubbles could be clearly observed in the form of blisters. These were large and rare for SG15 sample with high oxygen content, but numerous and small for SG1 and SG4 samples. In the case of porous crucibles the bottom surface of the samples was smooth and free of blisters. Therefore, to get best analytical separation it is crucial to select inner crucibles with porous spongy morphology, which prevents accumulation of gaseous reaction products at the melt/graphite interface.

In order to reveal the apparatus effect the SG1 and SG4 samples were simultaneously run in porous crucibles on both TC-436 and TC-436DR systems. **Figure 7** shows that the respective evolution curves differ markedly, viz. those of TC-436DR analyzsr are strongly tailed. The apparatus effect is caused by the difference in the flow systems of the analysers. The real evolution kinetics from the sample is not identical to that observed with IR detectors since the latter is influenced by intermixing of a gaseous sample with a helium stream as well as adsorption-desorption reactions in the oxidising heater. The transfer of analytic gas from the sample towards an IR detector can be characterised by a so-called apparatus function $E(t\text{-}t_o)$. This represents the response of the IR detector upon an impulse, produced within the crucible at the moment t_o. In the present work CO impulses were created by dropping small pieces of granular CuO or oxidised nibbled copper into the hot crucible ($T >$ 2500 K). **Figure 8** shows the normalised apparatus functions $E(t\text{-}t_o)$ of both TC-436 and TC-436DR systems. When operating in the so-called simultaneous mode, the TC-436DR system has the narrowest function $E(t\text{-}t_o)$, which is independent of the impulse mass. In the simultaneous mode

the analytical flow by-passes the oxidising heater and both CO and CO_2 are directly detected by IR cells (figure3). When analysing low oxygen contents, the catalytic oxidation of CO to CO_2 on rare earth CuO is, however, essential to enhance the sensitivity of detection. As can be seen from figures 8(b)-(c), the oxidising heater makes the apparatus function mass-dependent, which tends to be more tailed as the amount of analyte decreases. In the high range the functions $E(t\text{-}t_o)$ of both systems are very similar, but in the low range the tailing is much stronger for TC-436DR analyser.

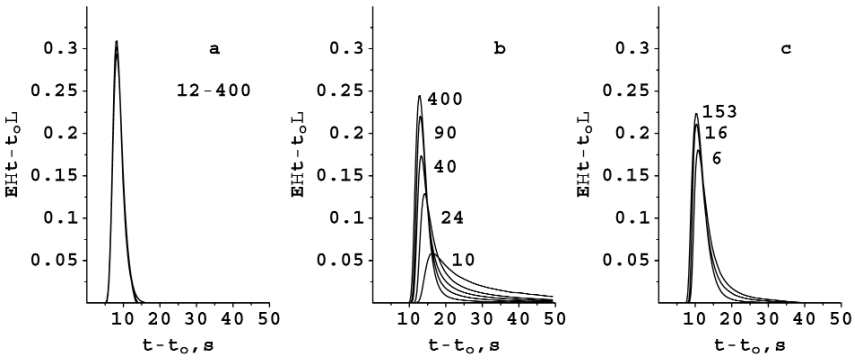

Figure 8. Apparatus functions: (a) TC-436DR, bypass of the oxidizing heater, CO-detector; (b) TC-436DR with oxidising heater, CO_2-detector; (c) TC-436 with oxidising heater; figures near curves refer to the oxygen mass in impulse (μg).

The observed effect seems to be of chromatographic nature. When passing over the bed of rare-earth CuO, the analyte molecules (CO, CO_2) undergo multiple adsorption-desorption reactions on the catalyst surface, which is usually found to be heterogeneous with adsorption sites of different energy. The more active the host site, the higher the activation barrier required for CO_2 molecule to desorb away and, therefore, the longer its residence time on the surface. The mass-dependence of the apparatus function arises from the blockage of most active sites which proceeds as the dosage of analyte increases. This effect also explains the enhanced peak tailing, caused by dividing the analytical flow before the oxidising heater, as it is made in TC-436DR system. In order to recalculate the "true" evolution curves, we suggest the following equation:

$$w_{\text{real}} = \left\{ a + \frac{q_{\text{m}} \cdot b}{(1 + b w_{\text{obs}})^2} \right\} \cdot \frac{d w_{\text{obs}}}{dt} + w_{\text{obs}} \qquad (5)$$

where w_{real} , w_{obs} [μg/s] are "real" and "observed" oxygen evolution rates, a [s], q_{m} [μg] and b [s/μg] are model parameters. Eq.(5) was derived by assuming that the accumulation of the analytic gas in the gas system of the analyser is represented as a balance between those released from the sample, those "washed out" by flowing helium and those adsorbed-desorbed by the catalyst. The model parameters a, q_{m} and b have to be determined for each instrument. **Table 4** contains the values of parameters, which were obtained by fitting Eq. (5) to the trailing sides of the apparatus functions of TC-436 and TC-436DR systems, used in this comparison. The correction was found to be essential for TC-436DR instrument rather than for TC-436 one. Figure 7 shows that the correction makes the evolution curves from different systems more similar. Nevertheless, whatever numerical procedure is employed, the deconvolution itself involves the noise enhancement. Therefore, it is desirable to improve the apparatus function by reducing the amount of catalyst and increasing the carrier gas flow rate.

Reduction sequence of oxide species. Before proceeding with quantitative analysis of corrected and scaled evolution curves, the appearance sequence of peaks from different oxide species must be derived. This can be made by

Table 4. Numerical description of the impulse-response curves.

Instrument	a [s]	q_{m} [μg]	b [s/μg]
TC-436DR without oxidizing heater	1.5	0	0
TC-436DR with oxidizing heater	2.4	15.6	1.4
TC-436 with oxidizing heater	2.4	3.6	0.8

calculating the gas bubble pressure p_{b}, developed due to carbothermal reduction of representative oxide species. As soon as p_{b} exceeds the total pressure p_{a} in the gas system of the analyser ($p_{\text{b}} > p_{\text{a}}$), the growth of the bubble on the surface of an oxide particle in the bulk of the melt becomes theoretically possible. The temperature at which is considered to be an equilibrium temperature of reduction.

As found by chemical and SEM/EDX analysis, the main oxide species in SG1 sample are alumina and silicates. SG4 material additionally contains spinel phase. Hence, the following reactions are considered to proceed during an analysis of SG1 and SG4 materials:

$$\mathrm{SiO_2(c)} + 2[\mathrm{C}]_{a_{\mathrm{C}}=1} \overset{\rightarrow}{\leftarrow} [\mathrm{Si}] + 2\mathrm{CO(gas)}\,, \qquad 6)$$

$$p_{\text{b}} = \left(K_p^{(6)} / a_{\text{Si}}\right)^{1/2}, \qquad (6a)$$

$$\mathrm{Al_2O_3(c)} + 3[\mathrm{C}]_{a_{\mathrm{C}}=1} \overset{\rightarrow}{\leftarrow} /2[\mathrm{Al}] + 3\mathrm{CO(gas)}\,, \qquad (7)$$

$$p_{\text{b}} = \left(K_p^{(7)} / a_{\text{Al}}^2\right)^{1/3}, \qquad (7a)$$

$$\mathrm{MgO(c)} + [\mathrm{C}]_{a_{\mathrm{C}}=1} \overset{\rightarrow}{\leftarrow} \mathrm{Mg(gas)} + \mathrm{CO(gas)}\,, \qquad (8)$$

$$p_{\text{b}} = 2 \cdot \sqrt{K_p^{(8)}}, \qquad (8a)$$

$$3\mathrm{Al_2O_3} \cdot 2\mathrm{SiO_2(c)} + 13[\mathrm{C}]_{a_{\mathrm{C}}=1} \overset{\rightarrow}{\leftarrow} 6[\mathrm{Al}] + 2[\mathrm{Si}] + 13\mathrm{CO(gas)}, \qquad (9)$$

$$p_{\text{b}} = \left(\frac{K_p^{(9)}}{a_{\text{Al}}^6 a_{\text{Si}}^2} \right)^{1/13}, \qquad (9a)$$

$$\begin{aligned} &MgO \cdot Al_2O_3(c) + 4[C]_{a_C=1} \\ &\overset{\rightarrow}{\leftarrow} 2[Al] + Mg(gas) + 4CO(gas), \end{aligned} \quad (10)$$

$$p_b = \frac{5}{4}\left(\frac{4K_p^{(10)}}{a_{Al}^2}\right)^{1/5} \quad (10a)$$

where p_b [Pa] is bubble pressure; a_{Al}, a_{Si} are Raoul's activities of aluminium and silicon in the melt, respectively; in both cases pure liquid aluminium or silicon must be selected as a reference state; $K_p^{(i)}$ are equilibrium constants of the corresponding reactions. The values of $K_p^{(i)}$ were derived from thermo-chemical data of pure substances [15]:

$$K_p^{(6)}[Pa^2] = \exp(89.925 - 90496.5/T - 2.677 \cdot \ln T), \quad (11)$$

$$K_p^{(7)}[Pa^3] = \exp(139.206 - 167583.0/T - 4.130 \cdot \ln T), \quad (12)$$

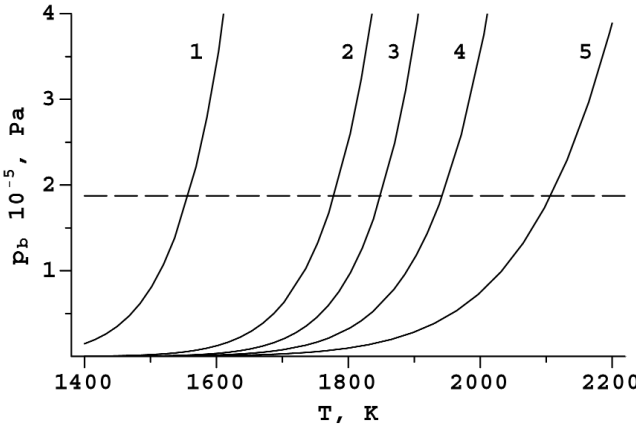

Figure 9. Gas bubble pressure p_b, developed due to carbothermal reduction of (1) silica, (2) mullite, (3) alumina, (4) spinel, and (5) magnesium oxide in graphite saturated liquid iron, containing 0.03 wt.% Al and 0.3 wt.% Si; the *dash line* refers to the pressure in the gas system of TC-436 analyser $p_a \approx 1.9 \cdot 10^5$ Pa.

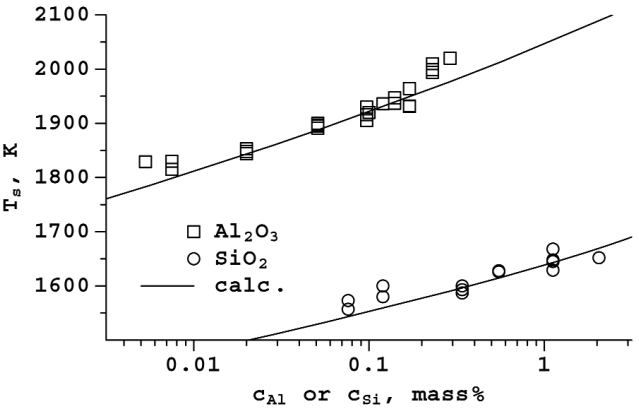

Figure 10. Temperatures of the reduction start of alumina and silica inclusions during GFA as a functions of Al or Si contents in iron; TC-436 analyser; experimental points were obtained at heating rates of 1.5-2 K/s; the thermodynamic calculation was made at $p_{CO} = 1.9 \cdot 10^5$ Pa.

$$K_p^{(8)}[Pa^2] = \exp(80.777 - 78415.8/T - 2.70 \cdot \ln T), \quad (13)$$

$$K_p^{(9)}[Pa^{13}] = \exp(588.939 - 680647.8/T - 17.098 \cdot \ln T), \quad (14)$$

$$K_p^{(10)}[Pa^5] = \exp(227.185 - 249879.7/T - 7.760 \cdot \ln T) \quad (15)$$

Writing down Eq.(6) – (10), it was assumed that silicon and aluminium dissolved from oxide phase into the melt while magnesium, having extremely low solubility in iron and high vapour pressure, evaporated into growing bubbles together with CO. For every reaction (Eq.(6)-(10)) the expressions for the bubble pressure p_b are given (Eq.(6a)-(10a)), which were derived from the law of mass action. For the reactions according to Eq. (6), (7) and (9) the pressure in the bubble was assumed to be equal to the partial pressure of CO, i.e. $p_{CO} = p_b$, while for reactions according to Eq.(8) and (10) it was composed from the pressures of both CO and Mg, i.e. $p_b = p_{Mg} + p_{CO}$. The following stoichiometric relations were also applied for evaporating components: $p_{Mg} = p_{CO}$ for Eq. (8) and $p_{Mg}/p_{CO} = 1/4$ for Eq.(10).

Raoult's activities of silicon $a_{Si} = x_{Si} \cdot \gamma_{Si}$ and aluminium $a_{Al} = x_{Al} \cdot \gamma_{Al}$ in graphite saturated melts were calculated using the associated solution model [16]. The total content of aluminium, declared in table 1, was taken for calculation. Since its value (≈0.03 wt.%) considerably exceeds the content of oxidic aluminium (≤ 0.0015 wt.%), such a substitution has a minor effect on the calculation results. This also holds for silicon. The calculated values of the bubble pressure, developed due to the reduction of silica, alumina, mullite and spinel, are shown in **figure 9** as a function of temperature. The calculation was made for the sample containing 0.03 wt.% Al and 0.3 wt.% Si. The dashed line stands for the value of the total pressure in the gas system of the analyser, which is equal to about $1.9 \cdot 10^5$ Pa. The following reduction sequence results from figure 9 (equilibrium values of T_s in K are in brackets):

SiO_2 (1560) → 3 $Al_2O_3 \cdot 2SiO_2$ (1780) → Al_2O_3 (1850) → $MgO \cdot Al_2O_3$ (1940) → MgO (2110).

The foregoing model suggests that the reduction temperature is determined by thermal stability of the oxide, chemistry of the sample matrix and pressure in the gas system of the analyser. The sample chemistry affects the activities of aluminium and silicon in the melt. The lower the activity, the higher the bubble pressure, and, therefore, the lower the thermal stability of the oxide. **Figure 10** shows the values of T_s of pure alumina and silica as a function of aluminium c_{Al} or silicon c_{Si} content of iron samples [10]. The temperature of the reduction start of alumina increases greatly with aluminium content. This fact must be taken into account when interpreting the evolution curves of different steel grades.

Deconvolution of oxide spectra. As no complete separation of GFA peaks usually occurs, the deconvolution of ox-

Table 5. Results of temperature ramped gas fusion analysis of SG1 and SG4 reference materials on TC-436 and TC-436DR systems (porous crucibles).

		c_O total	Peak parameters				Oxide type
		[µg/g]	n	T_{start} [K]	T_{ax} [K]	c_O [µg/g]	
SG1	TC-436	23.3	2	1800	1925	11.0	Alumina
	TC-436DR	21.0	2	1790	1920	12.1	
SG4	TC-436	26.0	3	1855	1980	10.5	Alumina
	TC-436DR	25.3	3	1850	1970	10.2	
	TC-436	26.0	4	1940	2035	5.0	Spinel
	TC-436DR	25.3	4	1945	2030	4.2	

ide spectra is essential to get the amount of each oxide species. This was made here using OxSep original software, described elsewhere [8]. The numerical procedure involves consecutive separation and subtraction of individual peaks from a total evolution curve, followed by minimization of the sum of squared residuals. The profile of individual peak was modelled in terms of the following empirical formula [8,9]:

$$y(T) = y_m \cdot \exp\left\{ E \cdot \frac{T - T_m}{T \cdot T_m} - \int_{T_m}^{T} e^{k - E/x} dx \right\} \qquad (16)$$

where T_m is temperature of the peak's maximum, y_m peak's height, k, E model parameters. This function was verified by treating the single peaks of pure alumina and silica inclusions in iron matrix [17].

Figure 11 shows peak-separated evolution curves of SG1 and SG4 materials as well as single-peak pattern of pure alumina in iron matrix. The arrows refer to the reference temperatures of alumina reduction, calculated from the thermodynamic model. The peaks which arise just above this point are attributed to alumina inclusions. The difference between SG1 and SG4 samples in the temperature of the alumina peak is likely due to Mg impurity, which was found in alumina inclusions of SG4 material by SEM/EDX analysis (see table 3). The alumina peak of SG4 material is followed by the smaller peak with the start temperature close to that predicted for spinel (1940 K). At higher temperatures (≥ 2100 K), which are characteristic of MgO species, no peaks are revealed. Thus, peaks number 3 and 4 of SG4 sample are assigned to alumina and spinel, respectively. In contrast to the synthetic iron sample where only an alumina peak is observed, the SG1 and SG4 samples yield distinct peaks below T_{start} of alumina. These are attributed to silicates. Their reduction starts at about 1650 K. This temperature is higher than the reference point predicted for pure SiO_2 (1560 K), but lower than that for $3Al_2O_3?2SiO_2$ (1780 K). The descripancy is likely due to the fact that silicate inclusions are of a variable composition, with silicon atoms partially substituted by aluminium. We thus assign peaks below T_{start} of alumina to alumosilicates while omitting the more detailed analysis of their type. This seems to be difficult with gas fusion technique.

The results of oxide separation are summarized in **table 5**. The reproducibility of oxygen content and peak's tempera-

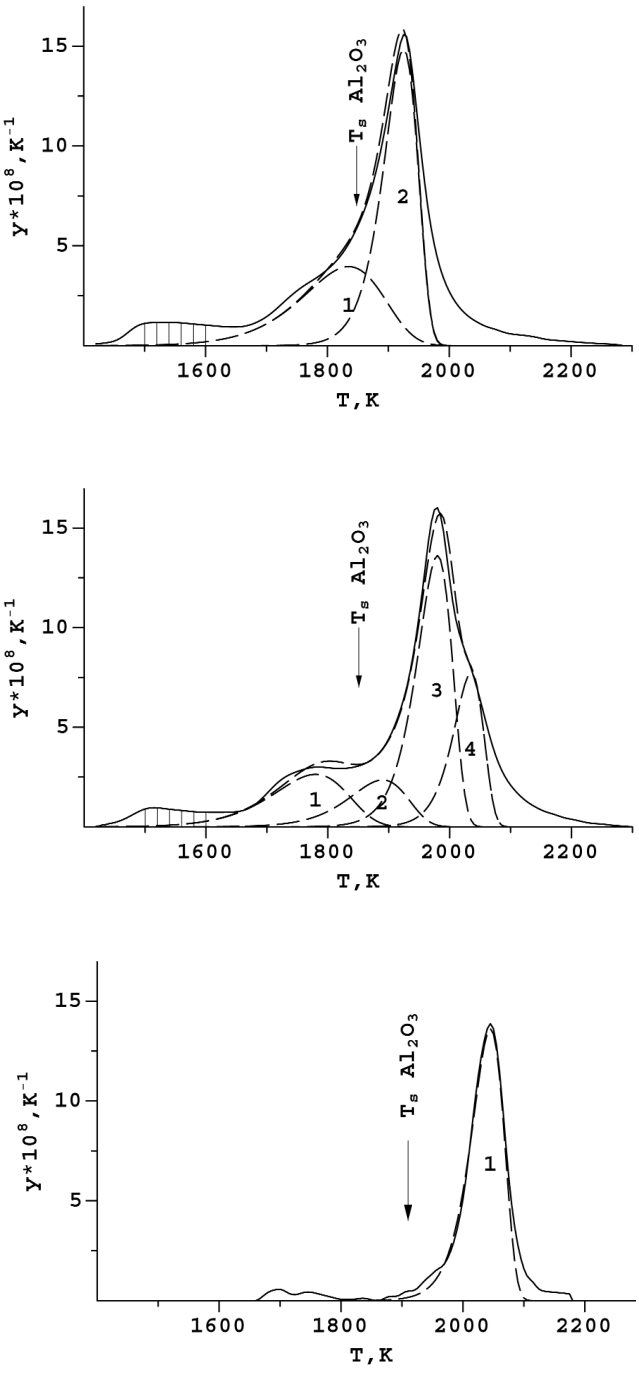

Figure 11. Peak-separated oxygen evolution curves from (a) SG1, (b) SG4 samples and (c) synthetic Fe-0.1 wt.% Al alloy with pure alumina inclusions; melting intervals are indicated by shading.

tures is satisfactory. The effect of the heating rate on the results of oxide separation was not very significant within the range 1.5-2.5 K/s although the peak overlapping generally tends to enhance with heating rate while peak temperatures tend to increase. About one half of the total amount of oxygen is found to be combined with alumina. This is in qualitative agreement with the results of the chemical analyses. However, these must be considered rather as a semi-quantitative since they give overestimated content of the total oxidic oxygen (40-50 μg/g). In general, the results of the three different methods are in reasonable agreement, providing quite a consistent picture of the chemical state of oxygen in the materials studied.

Conclusions

With recent progress in data processing as well as thermodynamic description of the gas fusion reactions, the oxygen speciation analysis is getting a better basis for steel cleanliness characterization. In order to achieve comparable results on different ?/N analysers, the analytical procedure must involve such steps as temperature calibration, blank correction and recalculation of the "true" evolution curves. Moreover, it is crucial to select the inner crucibles with porous spongy morphology, which prevents accumulation of gaseous reaction products at the melt/graphite interface and provides the best analytical separation. The oxide quantification must be performed numerically by consecutive separation and subtraction of individual peaks from the total evolution curve. Finally, the peaks are identified by calculating the reduction sequence of representative oxide species, which are expected from the results of SEM/EDX or other suitable methods.

Acknowledgment

This work was supported by the Saxon Ministry of Science and the Fine Arts.

(A2004130; received on 15 October 2004, in revised form on 20 February 2005)

Contact:
Dr. Pavel Krasovskii
Baikov Institute of Metallurgy and Materials Science
Russian Academy of Sciences
Leninskii pr. 49
Moscow, 117334 Russia
E-mail: krasovskii@rambler.ru ;

References

[1] R. Prumbaum, K. Orths: Gießerei Forschung, 31(1979), No. 2/3, 71.
[2] D. Sommer, K. Ohls: Fresenius Z. Anal Chem, 313 (1982), 28.
[3] P. Borek, Z. Chizhek, L.L Kunin: Zh. Anal. Khim., XLII (1987), No.1, 114.
[4] H. Hocquaux, R. Mieland: Revue de Metallurgie CIT, 89 (1992), No. 2, 193.
[5] A. Jungreithmeier, A. Viertauer, H. Preßlinger, K. Antligner: Radex Rundsch, (1993), No.3/4, 369.
[6] T. Ise, Y.Nuri, Y. Kato, T. Ohishi, H. Matsunaga: ISIJ Int., 38 (1998), No.12, 1362.
[7] R.W. Shaw, R. Bredeweg, P. Rossetto: J. Electrochem. Soc., 138 (1991), No.2, 582.
[8] K.V. Grigorovitch, A.M. Katsnelson, A.S. Krylov, AV. Vvedenskii: New approach to the fractional gas analysis application in metallurgy and material control using oxide separation software developed, Analytical Chemistry in the Steel and Metal Industries, 4th Intern. Conf. Proc., Luxembourg, 1995, p.527.
[9] K.V. Grigorovitch, P.V. Krasovskii, S.A. Isakov, A.A. Gorokhov, A.S. Krylov: Industrial Lab., 68 (2002), No.9, 3.
[10] P.V. Krasovskii, K.V. Grigorovitch: Metally, (2002), No.2, 108.
[11] S. Maeda, T. Soejima, T. Saito, H. Matsumoto, H. Fujimoto, T. Mimura: Shape control of inclusions in wire rods for high tensile tire cord by refining with synthetic slag, Steelmaking Conf. Proc., 1989, 379.
[12] T.B. Massalski: Binary alloy phase diagrams, A.S.M., Metal Park, 1986.
[13] Y.J. Bhatt, R.Venkataramani, S.P. Garg: J. Less: Common Met, 132 (1987), No.2, L21.
[14] T. Yoshioka, H. Okochi, R. Hasegawa: Material Transactions JIM, 34 (1993), No.6, 504.
[15] I. Barin: Thermochemical data of pure substances, VCH, 1995, 3rd edition.
[16] P.V. Krasovskii, K.V. Grigorovitch: Metally, 2001 (2001), 4, 337.
[17] P.V. Krasovskii, K.V. Grigorovitch: Industrial Lab., 68 (2002), 10, 17.